Acoustic propagation uncertainty in internal wave environments using an ocean-acoustic joint model

Fei Gao(高飞)[1,2], Fanghua Xu(徐芳华)[1,†], Zhenglin Li(李整林)[3], Jixing Qin(秦继兴)[4,‡], and Qinya Zhang(章沁雅)[1]

[1] *Department of Earth System Science, Ministry of Education Key Laboratory of Earth System Modeling, Institute for Global Change Studies, Tsinghua University, Beijing* 100084, *China*
[2] *Naval Research Institute, Tianjin* 300061, *China*
[3] *School of Ocean Engineering and technology, Sun Yat-Sen University, Zhuhai* 519000, *China*
[4] *State Key Laboratory of Acoustics, Institute of Acoustics, Chinese Academy of Sciences, Beijing* 100190, *China*

(Received 24 May 2022; revised manuscript received 31 July 2022; accepted manuscript online 16 August 2022)

An ocean-acoustic joint model is developed for research of acoustic propagation uncertainty in internal wave environments. The internal waves are numerically produced by tidal forcing over a continental slope using an ocean model. Three parameters (i.e., internal wave, source depth, and water depth) contribute to the dynamic waveguide environments, and result in stochastic sound fields. The sensitivity of the transmission loss (TL) to environment parameters, statistical characteristics of the TL variation, and the associated physical mechanisms are investigated by the Sobol sensitivity analysis method, the Monte Carlo sampling, and the coupled normal mode theory, respectively. The results show that the TL is most sensitive to the source depth in the near field, resulted from the initial amplitudes of higher-order modes; while in middle and far fields, the internal waves are responsible for more than 80% of the total acoustic propagation contribution. In addition, the standard deviation of the TL in the near field and the shallow layer is smaller than those in the middle and far fields and the deep layer.

Keywords: acoustic propagation uncertainty, ocean-acoustic joint model, internal wave, sensitivity analysis

PACS: 92.10.Vz, 43.30.Bp, 43.30.Re **DOI:** 10.1088/1674-1056/ac89dc

1. Introduction

In real oceans, especially in shallow water with internal waves, temporal and spatial variations of water medium properties, sea-surface motion, acoustic source depth and interference due to multi-path superposition are significant.[1,2] However, these environmental and acoustic parameters are usually not perfectly known. Therefore, the time-variant sound fields, calculated using an acoustic model with the uncertain environmental and acoustic parameters as input data, are also partially known,[3,4] and the acoustic propagation uncertainty is introduced for this affair.

Some modelling simulations and acoustic experiments on the acoustic propagation uncertainty have improved our understanding about it. The probability density function (PDF) are used to describe the acoustic propagation uncertainty and can be fitted by an exponential or a lognormal distribution in nonlinear internal wave environment.[5,6] The mean and standard deviation of TL are determined by the macrostate and microstate of the environment, respectively.[7] The polar plots of broadband TL are shown to be anisotropic with internal waves and continental shelfbreak, and the PDFs tends to become wider.[8,9] The sound field depends on multiple environmental parameters, among which the TL is most sensitive to the sediment sound speed and the water column sound speed field.[10,11] Moreover, some methods such as the polynomial chaos expansions, the uncertainty matrix, and the field shifting approximation are developed to quantify or approximate the acoustic propagation uncertainty.[12–15]

Summarizing the past research work, it is known that the acoustic propagation uncertainty is transferred from the environmental parameters. For the studies of acoustic propagation uncertainty in dynamic environments, the environmental parameters are usually obtained from the oceanographic measurements or by assigning priori PDFs (i.e., the upper and lower bounds, the distributions) to them. However, in real ocean acoustic experiment/survey,[16,17] several conductivity-temperature-depth (CTD) or sound-speed casts can not provide accurate sound speed field, and the moored temperature-depth (TD) continuous observation system is only valid for the waveguide environment near its deployment point. Meanwhile, the dynamic ocean environment parameters generated randomly by computer may deviate greatly from the actual internal wave process.

A feasible solution is to use the joint ocean-acoustic model, while the ocean model is to provide environmental data for input to the acoustic model. Some research work on ocean-acoustic modelling has been carried out and validated. It is reported that the ocean models can simulate the

†Corresponding author. E-mail: fxu@mails.tsinghua.edu.cn
‡Corresponding author. E-mail: qjx@mail.ioa.ac.cn
© 2023 Chinese Physical Society and IOP Publishing Ltd

ocean states as well as dynamical processes well, such as internal waves, fronts, and eddies, and provide high resolution data for the acoustic studies.[18–20] What's more, some ocean-acoustic modelling systems are used for underwater security applications.[21,22] Several recent studies have pointed out that the ocean models may not be best for acoustics,[23,24] due to the limitation of model resolution, physical approximations, as well as computational efficiency. Nevertheless, the ocean modelling has its unique advantages, and meanwhile there is no effective technological alternative currently. Thus, the ocean-acoustic modelling will continue to be an important direction for the underwater acoustic research and applications for some time to come.

In this paper, the acoustic propagation uncertainty is investigated using an ocean-acoustic joint model, the TL sensitivity to dynamic environmental parameter is quantified, and the relevant physical mechanisms are interpreted by the coupled normal mode theory. This paper is organized as follows. In Section 2 we introduce the ocean-acoustic joint model and numerical setups. The results of ocean modelling, TL sensitivity and uncertainty analysis are presented in Section 3. The interpretation and discussion for the results are provided in Section 4. The summary and main conclusions are given in Section 5.

2. Model and theory

2.1. Ocean-acoustic joint model

The ocean-acoustic joint model is developed for subsequent acoustic propagation research, consisting of three parts as shown in Fig. 1: the ocean model, the acoustic model, and the joint module. The ocean model is utilized for internal wave simulations and provides dynamic CTD data for the joint module. The joint module acts as a connector between the ocean model and the acoustic model, which converts the CTD data into sound speed and make them suitable for acoustic calculation. The acoustic model receives the sound speed data from the joint module before sound field calculation.

The ocean model is set up for internal wave simulation using the generalized operator model of the ocean (GOMO). The GOMO is a simple operator library for the decoupling of parallel computing and ocean modelling,[25,26] with the sigma coordinate, free-surface and the capability of non-hydrostatic calculation, etc. The tidal flow and complex geometry are important roles to generate internal wave, and the internal waves are ubiquitous near the continental slopes and shelves,[1,27] of which the main physical mechanism is that the periodic tidal currents drive the interaction of stratified seawater with seafloor topography. Thus, the GOMO is an ideal tool for generation of dynamic internal wave by setting periodic tidal currents through its open lateral boundary with a continental slope lower boundary, and the CTD data output by the model provides an estimation of the dynamic ocean state.

The joint module receives the CTD data from the ocean model and calculates their corresponding sound speed values, based on the empirical formula.[28] Since the ocean model and the acoustic model are two separate models and the output of the former should be suitable for the input requirements of the latter, another function of the joint module is to perform interpolation calculations.

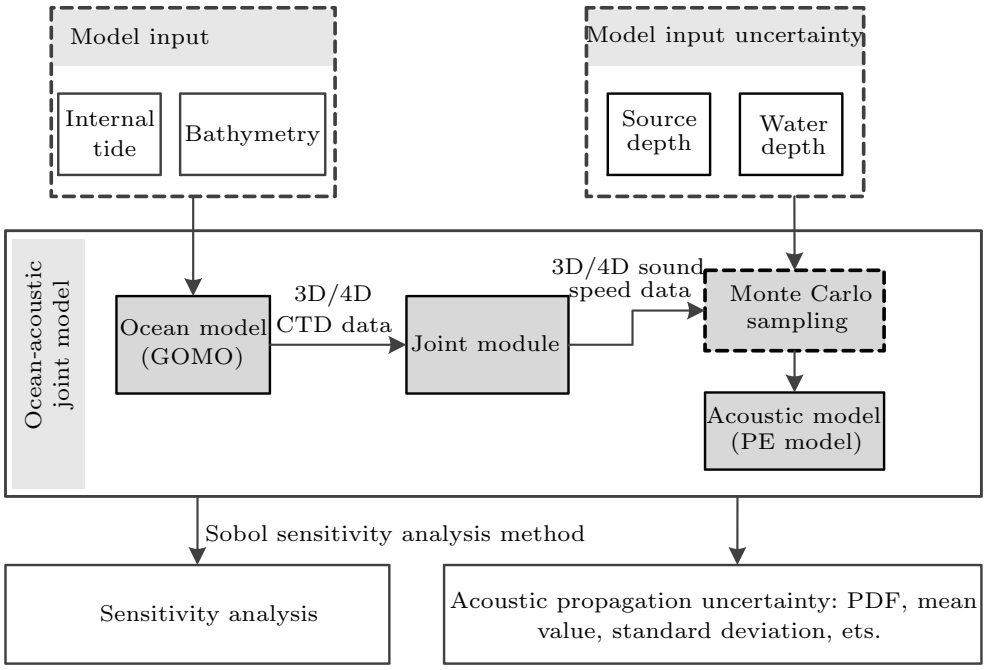


Fig. 1. Flowchart of the simulation and research process.

The acoustic propagation simulations are conducted using the model based on parabolic equation (PE) theory.[29] The PE model are adapted well to marine environments with range-dependent sound speed and water depth, and can also achieve high precision, calculation efficiency and stability, which makes it suitable for analyzing acoustic propagation in the environments with internal waves and continental slops.

2.2. Input uncertainty specification and numerical setups

An idealized two-dimensional (r, z) environment model is constructed for studying dynamic internal wave generation and acoustic propagation uncertainty, which is shown in Fig. 2. The horizontal range for simulation is 8 km. The bottom tomography is featured with a slope, of which the water depth in the range 2 km–6 km is set as a sine function and given by

$$h(r) = \begin{cases} 110, & r \le 2\ \text{km}, \\ 110 + 90\sin(\pi r/2L), & 2\ \text{km} < r < 6\ \text{km}, \\ 200, & r \ge 6\ \text{km}, \end{cases} \tag{1}$$

where $L = 4$ km is the slope width. The acoustic propagation uncertainty caused by the dynamic environment is the main study issue in this paper. Three stochastic parameters are thought to be caused by the dynamic environment: the internal wave, source depth, and the water depth.

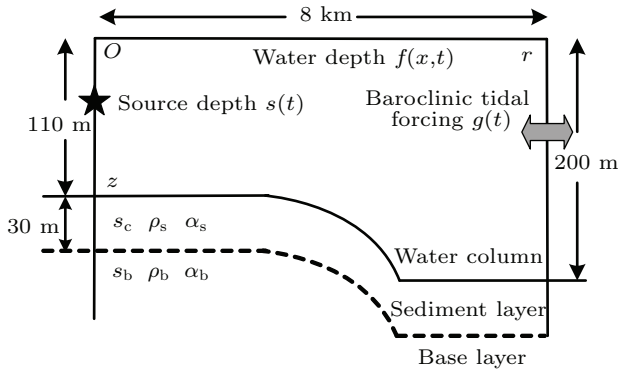


Fig. 2. The schematic of simulation domain for the ocean-acoustic joint model.

The first uncertain information is associated with the time-evolution and range-dependent sound speed field in the internal wave environment. The sound speed is calculated based on the CTD data from the ocean model as mentioned above. The internal waves are generated by tidal forcing from the boundary using the ocean model, and the periodic baroclinic M_2 tidal currents are imposed through the east open boundary, which are given by

$$u(z,t) = U_0\varepsilon(z)\cos(2\pi t/T), \tag{2}$$

where U_0, $\varepsilon(z)$, and T are the amplitude, vertical structure function, and period of the M_2 tidal currents, respectively.

The time-varying sound speed field $\xi_1(t)$, in the internal wave environment, can be described with the definite field $\boldsymbol{c}_0$ and perturbation part $\delta\boldsymbol{c}(t)$:[30]

$$\xi_1(t) = \boldsymbol{c}_0 + \delta\boldsymbol{c}(t), \tag{3}$$

where $\xi_1(t)$ provides the sound speed field for the acoustic model, $\boldsymbol{c}_0$ can be calculated using the initial temperature field $\boldsymbol{T}_0$, and $\boldsymbol{T}_0$ provides the initial state for the ocean model. The time-varying temperature field $\boldsymbol{T}(t)$ is the output of the ocean model, and $\xi_1(t)$ can be obtained with $\boldsymbol{T}(t)$ through the joint module in Fig. 1.

The second uncertain parameter for the acoustic simulation is the source depth, given by

$$s(t) = z_s + \xi_2(t), \tag{4}$$

which is comprised of the definite part z_s and the uncertain part $\xi_2(t)$. In the real ocean, the underwater source would not remain stationary relative to the seafloor, whereas it will be influenced by the background currents and the density perturbation due to the dynamic internal wave.

The third uncertain part parameter for the acoustic simulation is the water depth, which can also be written as the definite part $h(r)$ and the uncertain part $\xi_3(t)$:

$$f(r,t) = h(r) + \xi_3(t), \tag{5}$$

where $h(r)$ [seen in Eq. (1)] provides the initial water depth for the ocean model. In real conditions, there are multiple factors for the uncertainty of $\xi_3(t)$, e.g., the tidal range, the surface elevation anomaly by the internal waves, and the measurement errors from marine survey.

Meanwhile, acoustic propagation is relatively sensitive to the random sea-surface motion.[31] The rough surfaces of different sea states change the propagating angle and lead to stochastic scattering. As the ocean model cannot simulate the sea states and wind speed, the acoustic propagation uncertainty caused by the sea-surface motion is not investigated in this paper.

The initial field of the ocean model is provided using the average profile of several CTD casts in the South China Sea. The thickness of shallow mixed layer is about 25 m, and the strong thermocline exists at 25–55 m, while the temperature decreases slowly from 55 m downward (Fig. 3(a)). The buoyancy frequency profile $N(z)$ is presented in Fig. 3(c), calculated based on the equation $N^2(z) = -g\rho^{-1}\partial\rho/\partial z = -g(\alpha_T\partial T/\partial z + \beta_S\partial S/\partial z)$, where α_T and β_S are the thermal expansion coefficient and haline contraction coefficient, respectively. The maximum buoyancy frequency occurs at the depth of 40 m. Since the vertical variation of the salinity profile (Fig. 3(b)) and its effects on the buoyancy frequency and sound speed are much smaller compared to the temperature profile, the salinity is set as a constant (equals 33.5 psu) to improve simulation efficiency.

To preserve the internal waves with small amplitudes and also to satisfy the Courant–Friedrichs–Lewy (CFL) condition,

the horizontal and vertical grid resolutions of the ocean model are set to be 10 m and 2 m, respectively, and the temporal resolution for computing is set as 3 s. The non-hydrostatic pressure solver for the vertical momentum equation is switched on, for higher computing accuracy and stability.[32] The open conditions are used for the eastern boundary with periodic tidal currents, while the radiation conditions are used for the western boundary. The Coriolis parameter is ignored. A temperature advection scheme is used for the ability of internal wave mixing simulation. The detailed parameters settings for the ocean model are outlined in Table 1.

The bottom features of the waveguide for the acoustic model is idealized to be two layers (Fig. 2), with a 30 m sediment layer over the base layer. The source is set to be on the continental shelf area, to allow the sound waves to propagate in the downwards direction. The vertical computing grid $\mathrm{d}z$ should be less than $\lambda/20$ and the horizontal grid $\mathrm{d}r$ is set as $10\mathrm{d}z$, where λ is the acoustic wavelength. The detailed parameters settings for the ocean model are outlined in Table 1.

For internal waves driven by periodic tides, the internal waves and their corresponding temperature field $\boldsymbol{T}(t)$ and sound speed field $\xi_1(t)$ are also periodic.[33] Thus, the first uncertain parameter $\xi_1(t)$ is defined to be uniformly distributed in an M_2 tidal period T, i.e., $\xi_1(t) \sim U(\xi_1(t),\ \xi_1(t+T))$. The uncertain source depth $\xi_2(t)$ is specified as normal distributed with mean zero and standard deviation 5 m, and its variation range is limited in the range from -5 m to 5 m, i.e., $\xi_2(t) \in [-5,5]$. The uncertain water depth $\xi_3(t)$ is specified as normal distributed with mean zero and standard deviation 2.5 m, and its variation range is limited in the range from -2 m to 2 m, i.e., $\xi_3(t) \in [-2,2]$.

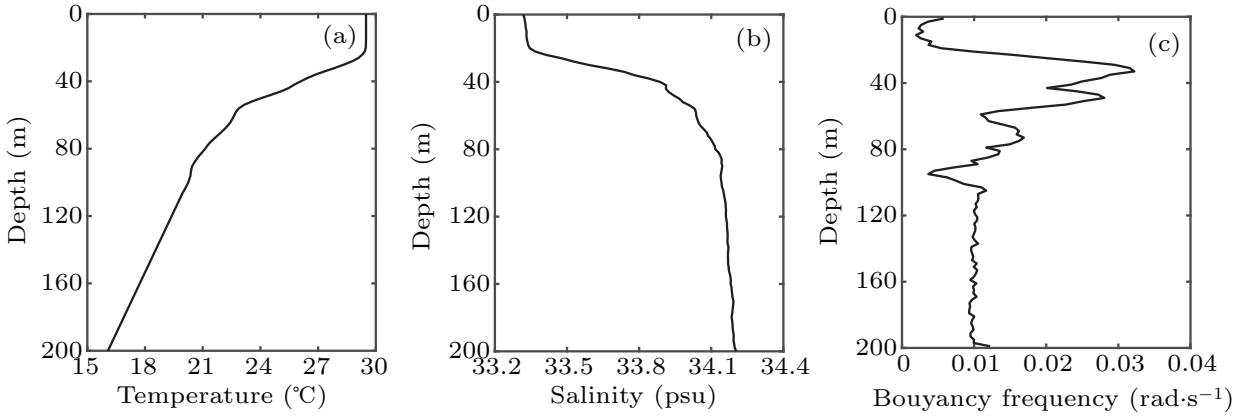


Fig. 3. Typical background profiles of temperature (a), salinity (b), and buoyancy frequency (c) for the ocean model initialization.

Table 1. The ocean-acoustic model parameters setups.

Part 1: Ocean model parameters	
Horizontal, vertical viscosity	5×10^{-4} m^2/s, 1×10^{-4} m^2/s
Horizontal, vertical diffusivity	5×10^{-5} m^2/s, 1×10^{-5} m^2/s
Thermal expansion coefficient	$2.\times10^{-4}$ °C^{-1}
Free surface	true
Bottom drag coefficient	3×10^{-3}
Horizontal, vertical grid resolution	10 m, 2 m
Temporal computing resolution	3 s
Sponge boundary condition	100
Part 2: Joint module parameters	
Sound speed algorithm	Chen–Millero
Part 3: Acoustic model parameters	
Source frequency, depth	300 Hz, 10 m, 60 m
Sound speed, density, attenuation coefficient and thickness in sediment layer	1550 m/s, 1.5 g/cm^3, 0.25 dB/λ, 30 m
Sound speed, density, attenuation coefficient in base layer	1700 m/s, 2.0 g/cm^3, 2.5 dB/λ
Horizontal, vertical computing resolution	2.5 m, 0.25 m
Part 4: Monte Carlo sampling parameters	
$\xi_1(t)$	uniform distribution $U(\xi_1(t), \xi_1(t+T))$
$\xi_2(t) \in [-5,5]$	normal distribution $N(0,5)$
$\xi_3(t) \in [-2,2]$	normal distribution $N(0,2.5)$

3. Results and analysis

3.1. Periodic and dynamic internal wave environment

The ocean model is run for 7 days (about 14 M_2 tidal cycles) to produce internal wave data. The tidal amplitude U_0 and period T are set to be 0.12 m/s and 12.42 h, and the vertical structure function $\varepsilon(z) = \cos(z\pi/3H)$, where $H = 200$ m is the water depth of the eastern boundary. The forcing tidal currents decrease to $U_0/2$ near the bottom boundaries.

The temperature anomaly $T' = T - T_0$, resulted from the perturbation of the internal wave, at $z = 40$ m of the simulation results for the first five days is presented in Fig. 4, in which the left panel is the sine curves of the baroclinic tidal currents at $z = 0$ m, and T_0 ($= 26.096$ °C) is the initial temperature at $z = 40$ m. The results show that the temporal variation of temperature anomaly section becomes periodic after 1.5 days (3 M_2 tidal cycles), whose period is also equal to the M_2 tidal cycle. It is also shown that the internal waves on the continental slope are stronger than those on the west and east sides.

Four snapshots of the temperature field and its associated sound speed field are shown is Fig. 5, which are typical to represent the temperature anomaly features during an M_2 tidal period. The sound speed value in water depends on the salinity, temperature, and pressure. The temperature is the main factor in the shallow water, which results in the similar distribution features of temperature field and sound speed field.

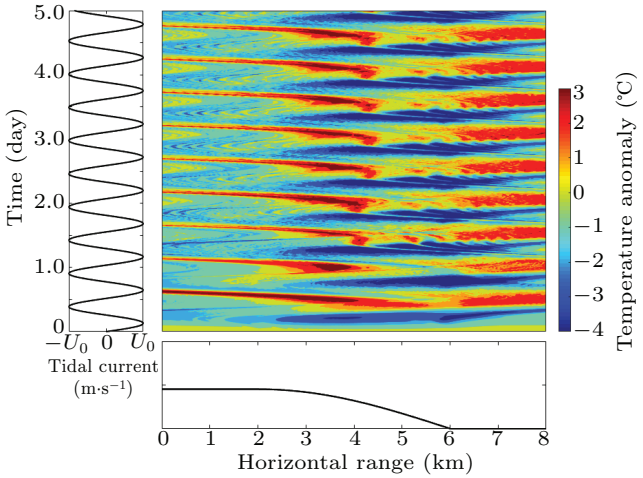


Fig. 4. The left panel is the plot the of the M_2 periodic tidal currents. The right panel is the contour plot of the temperature anomaly at $z = 40$ m versus time. The lower panel is the plot of the water depth.

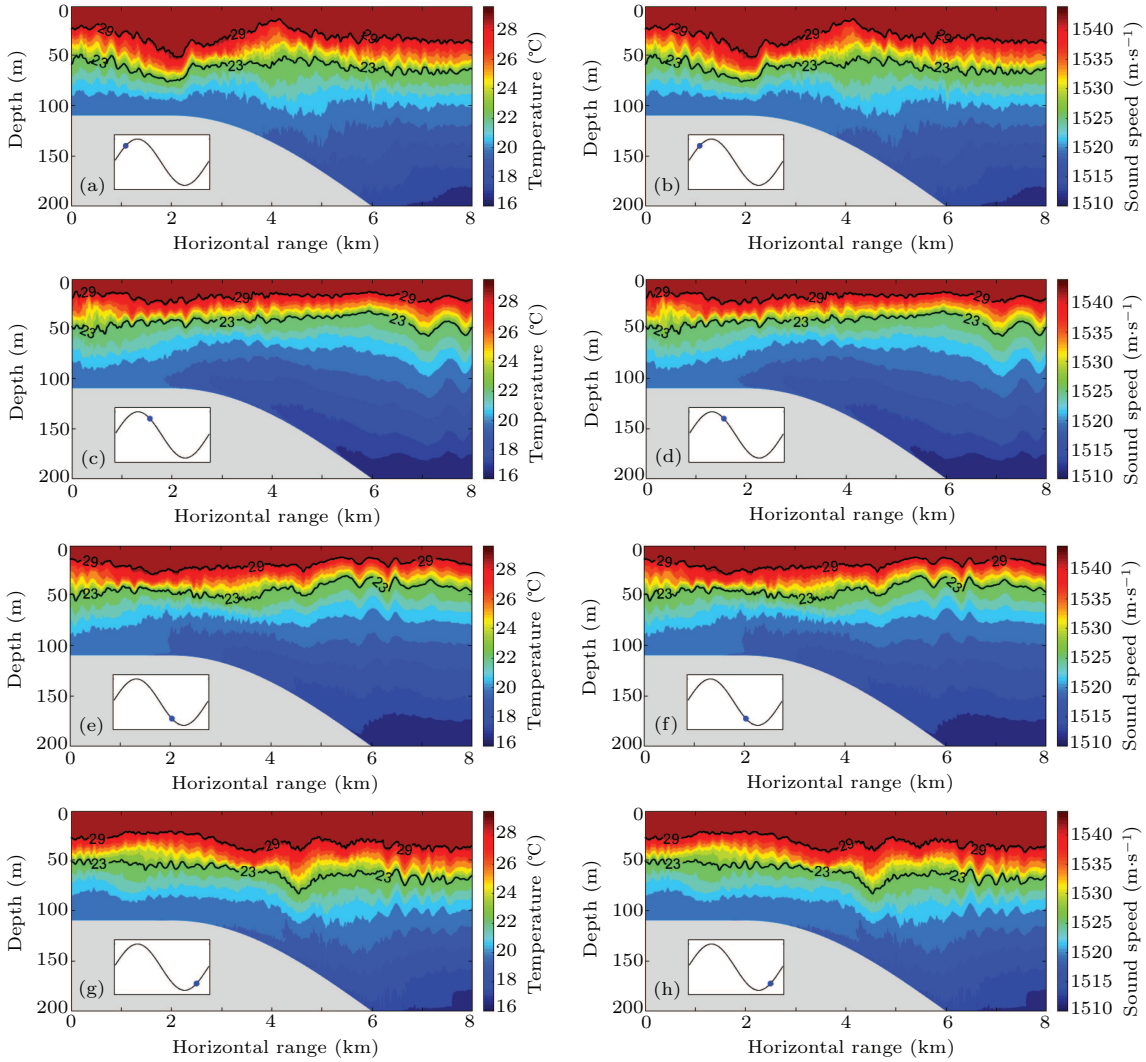


Fig. 5. Four snapshots of the temperature field and sound speed field at $t = 51.2$ h [(a), (b)], $t = 54.3$ h [(c), (d)], $t = 57.5$ h [(e), (f)] and $t = 60.5$ h [(g), (h)]. The rectangle blanks show the boundary tidal forcing in an M_2 tidal period.

During the flood tide (Figs. 5(a) and 5(c)), the boundary tidal forcing is toward the west and acts continuously on the water column, with the eastward velocity components weakening and the westward velocity components enhancing, resulting in western horizontal velocity (Fig. 6(a)). Thus, the internal waves propagate westward and the cold water moves upward along the continental slope, which causes significant variation to the temperature and sound speed field. During the ebb tide (Figs. 5(e) and 5(g)), the boundary tidal forcing is toward the east, and leading to eastern horizontal velocity (Fig. 6(c)). The vertical displacements of the internal waves are associated with the vertical velocity, and the positive and negative velocity correspond to the crest and tough of the internal waves. It is found that the positive and negative vertical velocity zones are interleaved in the horizontal direction (Figs. 6(b) and 6(d)), which are consistent with the vertical displacements of the internal waves (Figs. 5(c) and 5(g)).

The temperatures of the thermocline interfaces are 29 °C and 23 °C (Fig. 3(a)), whose contours are marked in Fig. 5. The buoyancy frequency of the thermocline layer is the largest as shown in Fig. 3(c), which provides good conditions for internal wave generation. The internal wave characteristics can be analyzed based on the Froude number and slope parameter.[34,35] The Froude number Fr and slope parameter γ are given by $Fr = U/(N_{\max}H)$ and $\gamma = \partial h/\partial x[(\omega^2 - f^2)/(N^2 - \omega^2)]^{-1/2}$, where U is the current speed, H is the tomography height, ω is the angular frequency of tides, and f is the Coriolis parameter. According to the numerical setups of the ocean model, $Fr_{\max} = 0.044ll1$ and $\gamma_{\max} = 3.2$, which indicate that the nonlinear waves and lee waves coexist and the slope enable the generation and propagation of waves beams. As shown in Fig. 5, the internal wave perturbation is significant, and the nonlinear internal waves and soliton internal wave are generated and propagate during an M_2 tidal cycle.

There are mainly two mechanisms for the excitation and control of the internal waves, the tidal forcing temporal and spatial variations. The tidal forcing F can be written as[36,37] $\mathrm{d}F/\mathrm{d}t = \partial F/\partial t + U\nabla F$. The local time partial term $\partial F/\partial t$ is controlled by the boundary driven M_2 tidal flow, of which the strength and direction changes over a tidal cycle. The advection term $U\nabla F$, affecting the vertical movement of water volume, is governed by both the tidal flow and bottom depth, and U varies spatially due to the continental slope.

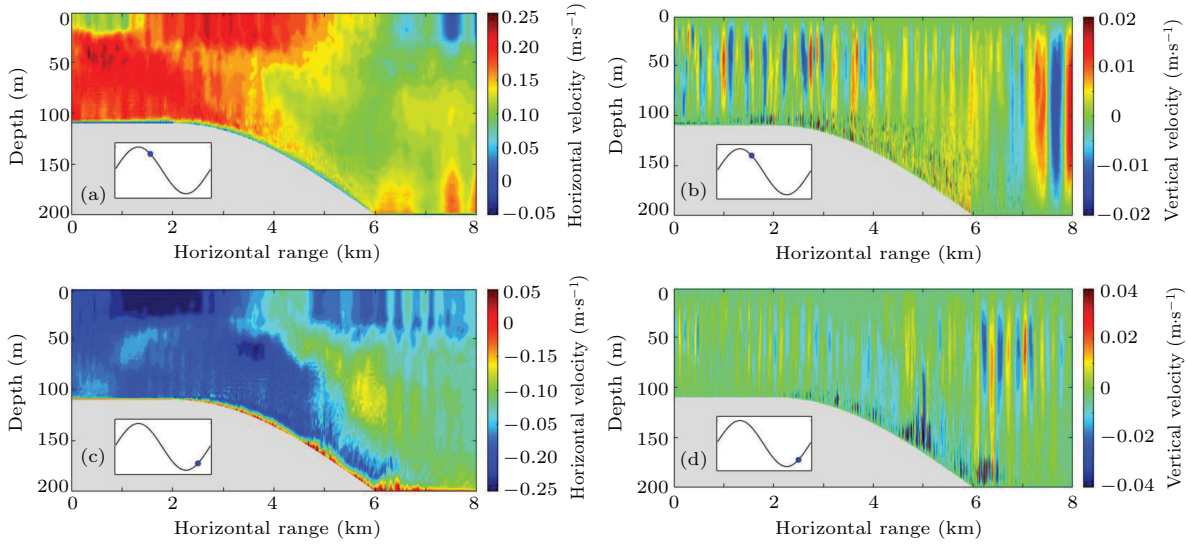


Fig. 6. Two snapshots of the horizontal and vertical velocity field at $t = 54.3$ h [(a), (b)] and $t = 60.5$ h [(c), (d)]. The rectangle blanks show the boundary tidal forcing in an M_2 tidal period.

3.2. TL sensitivity analysis

The dynamic waveguide environment includes three uncertain parameters (i.e., internal wave ξ_1, the source depth ξ_2, and the water depth ξ_3), which are necessary input data for the acoustic model in TL calculations. Since the physical mechanisms and contributions of different parameters affecting the acoustic propagation are different, it is necessary to analyze the sensitivity of TL to them. The Sobol method is widely used for the sensitivity analysis of strongly nonlinear and computationally complex model.[13,38] It is a global sensitivity analysis method that can provide quantitative index to describe the sensitivity of different input parameters and the correlation between them.

The TL, calculated by using the PE acoustic model, can be given by

$$\mathrm{TL}(z,r,t) = F(\xi_1, \xi_2, \ldots \xi_N), \tag{6}$$

where z, r, and t are the depth, range, and time, respectively. The function $F(\cdot)$ is the acoustic model, which refers to the PE model of the ocean-acoustic joint model. N is the number of variables $\xi_i(t)$, $1 \le i \le N$. If M Monte Carlo simulations are conducted over the time domain of the variables, the total

standard deviation (std) of TL(z,r) is composed of a series of std components

$$D=\sum_{i=1}^{N}D_i+\sum_{i=1,i<j}^{N-1}D_{i,j}+\cdots D_{1,2,\ldots,N} \tag{7}$$

where D is the total std. By sampling in the dimension of $\xi_i(t)$, the std D_i can be obtained. $D_{i,j}$ refers to the std resulted from the interaction of $\xi_i(t)$ and $\xi_j(t)$. $D_{1,2,\ldots,N}$ is the std resulted from all variables. By dividing D and substituting the Sobol index in Eq. (7), the normalized form of Eq. (7) can be obtained as

$$\sum_{i=1}^{N}S_i+\sum_{i=1,i<j}^{N-1}S_{i,j}+\cdots S_{1,2\ldots,N}=1, \tag{8}$$

where $S_i=D_i/D$ and $S_{i,j}=D_{i,j}/D$ are the 1st and 2nd order Sobol indices, respectively. When the variables $\xi_i(t)$ are statistic independent, the Sobol indices above 2nd order can be ignored.

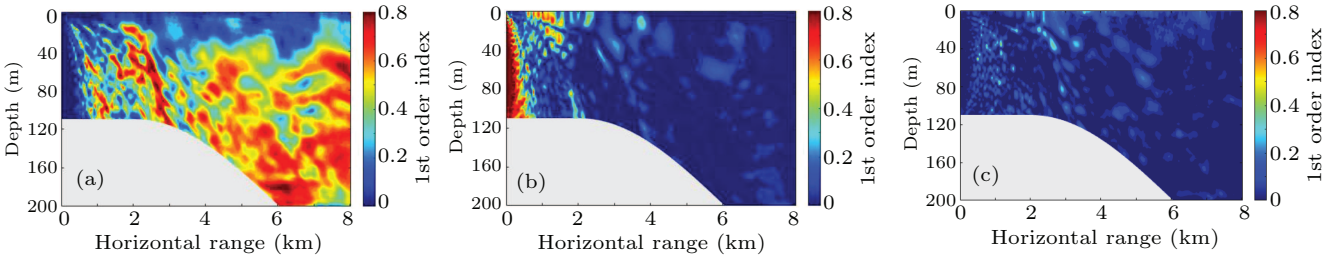


Fig. 7. The first-order index of TL sensitivity versus range and depth due to different uncertain parameters, (a) internal wave ξ_1, (b) source depth ξ_2, and (c) water depth ξ_3.

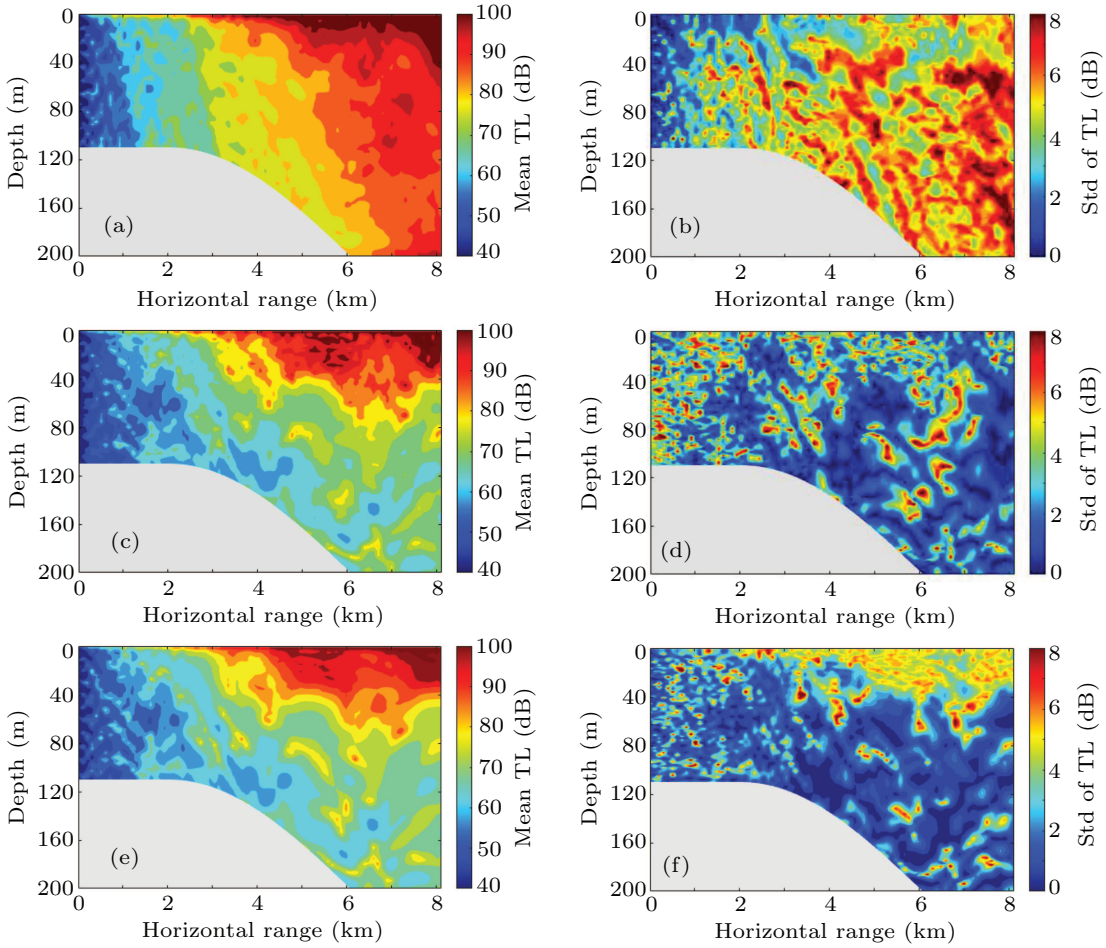


Fig. 8. The mean and std of TL versus range and depth due to different uncertain parameters: [(a), (b)] internal wave ξ_1, [(c), (d)] source depth ξ_2, [(e), (f)] water depth ξ_3.

In this paper, three uncertain parameters are considered, i.e., $N=3$ in Eqs. (6)–(8). $M=10000$ samples are drawn for all uncertain parameters using the Sobol quasi-random point set, and $M=10000$ samples are drawn for each parameter. Thus, totally 40000 simulations are conducted using the PE model. The 1st order Sobol index of TL sensitivity versus range and depth is computed as shown in Fig. 7.

It can be seen that the 1st order index is not mono-

tonic, whereas oscillates with range and depth. As shown in Fig. 7(a), the 1st order index is greater than 0.5 in most areas, and the sensitivity index in the near field and the mixed layer is relatively small, which increases to 0.7–0.8 with range and depth. In Fig. 7(b), for the near sound field in the range less than 0.5 km, the sensitivity index of the source depth is larger than 0.8, and it decreases rapidly to nearly 0 as the range increases.

By comparing the sensitivity index of the three uncertain parameters, it is observed that the internal wave is the main factor affecting the TL in most areas, while the source depth has the largest effect on the near-field TL. The water depth effects the TL weakly (Fig. 7(c)), whose sensitivity is less than 0.2 in most areas.

According the Sobol sensitivity method, the 1st order Sobol index is the ratio of the std caused by a single uncertain parameter to the total std. We analyze the characteristics of the std distribution due to different uncertain parameters. Figure 8 shows the mean and std distribution of the TL field for the source depth $z_s = 60$ m, obtained from $M = 10000$ samples for each of the three uncertain parameters. Figures 8(a) and 8(b) are obtained with the uncertain internal wave ξ_1, while $\xi_2 = 0$ and $\xi_3 = 0$. Figures 8(c) and 8(d) are obtained with the uncertain source depth ξ_2, while $\xi_1(t) = \xi_1(0)$ and $\xi_3 = 0$. Figures 8(e) and 8(f) are obtained with the uncertain water depth ξ_3, while $\xi_1(t) = \xi_1(0)$ and $\xi_2 = 0$.

The mean TL of the uncertain internal wave is the maximum, due to acoustic mode coupling and energy transfer between modes[39] (Fig. 8(a)). The "mudslide effect" occurs as the acoustic waves propagate down the slope (Figs. 8(c) and 8(e)), and the mean TL in the deeper layer is smaller to the shallow surface layer.

Several features can be observed by comparing the std distribution in Figs. 8(b), 8(d), and 8(f). Firstly, the std caused by the uncertain internal wave is great in most area (Fig. 8(b)), and the std increases significantly with range, corresponding well with the 1st order index distribution in Fig. 7(a). Secondly, in the near field, the std caused by the uncertain source depth (Fig. 8(d)) is larger than that by the uncertain internal wave and water depth, proving that the uncertain source depth is the main factor contributing to acoustic propagation uncertainty. Thirdly, the uncertain water depth can also lead to acoustic propagation uncertainty, but the effect is weaker compared to internal wave and source depth.

3.3. TL uncertainty analysis

In the case that all the three parameters are uncertain, sound fields are calculated using $M = 20000$ Monte Carlo samples for source depths of 10 m and 60 m, respectively. The mean and std of TL(z, r) are obtained for the study in this section.

Figure 9 shows the mean and std of TL versus range. It is observed that the mean TL for the 60-m source depth is significantly smaller than that for 10-m source depth. Figure 10 shows the std of TL versus range for the source depths of 10 m and 60 m. The std of TL varies from 2 dB to 7 dB, and it can be seen that it increases with range because the slope of the 2nd order polynomial fitting curve is greater than 0.

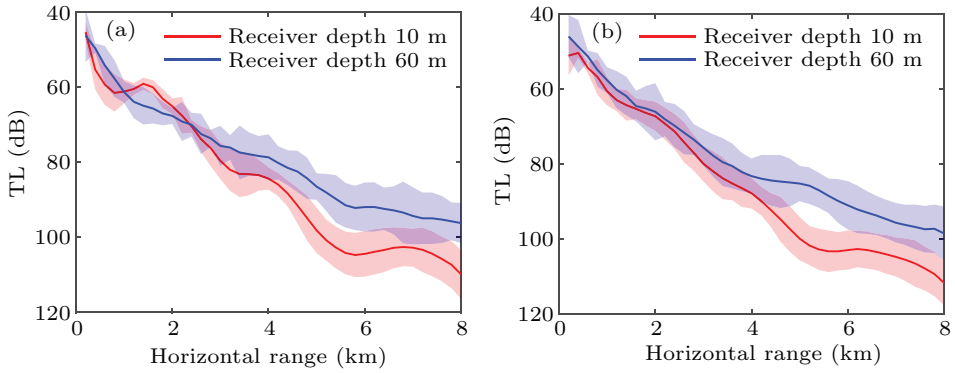


Fig. 9. Mean and std of TL versus range for the source depths of 10 m (a) and 60 m (b). The curves represent the mean TL and shadowed areas represent corresponding std.

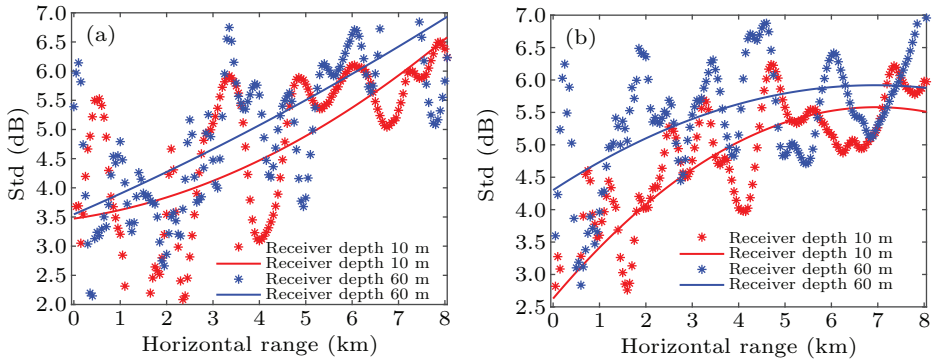


Fig. 10. Std of TL versus range for the source depths of 10 m (a) and 60 m (b). The curves are the 2nd order polynomial fitting with asterisks.

Figure 11 shows the mean and std of TL versus depth for the receiver ranges 1 km, 4 km, and 7 km, respectively. It is observed that the mean TL decreases noticeably with depth. The reason is that low-order normal modes can be efficiently excited when the source depth is below the thermocline. The std of TL in the shallow layer is relatively small and increases rapidly from the surface downward.

The std is a quantitative indicator of the TL variation due to the uncertain environment. According to the distribution characteristics of the std analyzed above, it can be concluded that the TL is more sensitive to the dynamic waveguide environment at larger receiver ranges and depth, which is similar to the distribution characteristics of the 1st Sobol index of the TL for the internal waves (Fig. 7(a)).

The PDFs of the TL at three depths and three ranges for the source depth 60 m are shown in Fig. 12. The dynamic environments result in significant sound field perturbations, and the PDFs show wide TL distributions with perturbations of up to 40 dB. By comparing the mean and std of the TL for different ranges and depths, it can be seen that the PDFs correspond well to the mean and std of the TL characteristics analyzed above.

It is seen that the PDFs of the TL at the receiver range 1 km can be best fitted by an exponential distribution (Figs. 12(a), 12(d), and 12(g)), while tend to be a normal distribution at the receiver range 7 km (Figs. 12(c), 12(f), and 12(i)), which is consistent with the results of previous studies.[5]

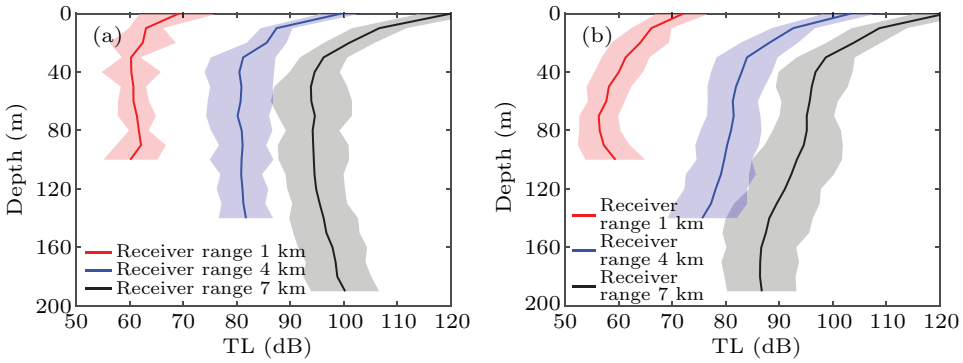


Fig. 11. Mean and std of TL versus depth for the source depths of 10 m (a) and 60 m (b). The curves represent the mean TL, and shadowed areas represent corresponding std.

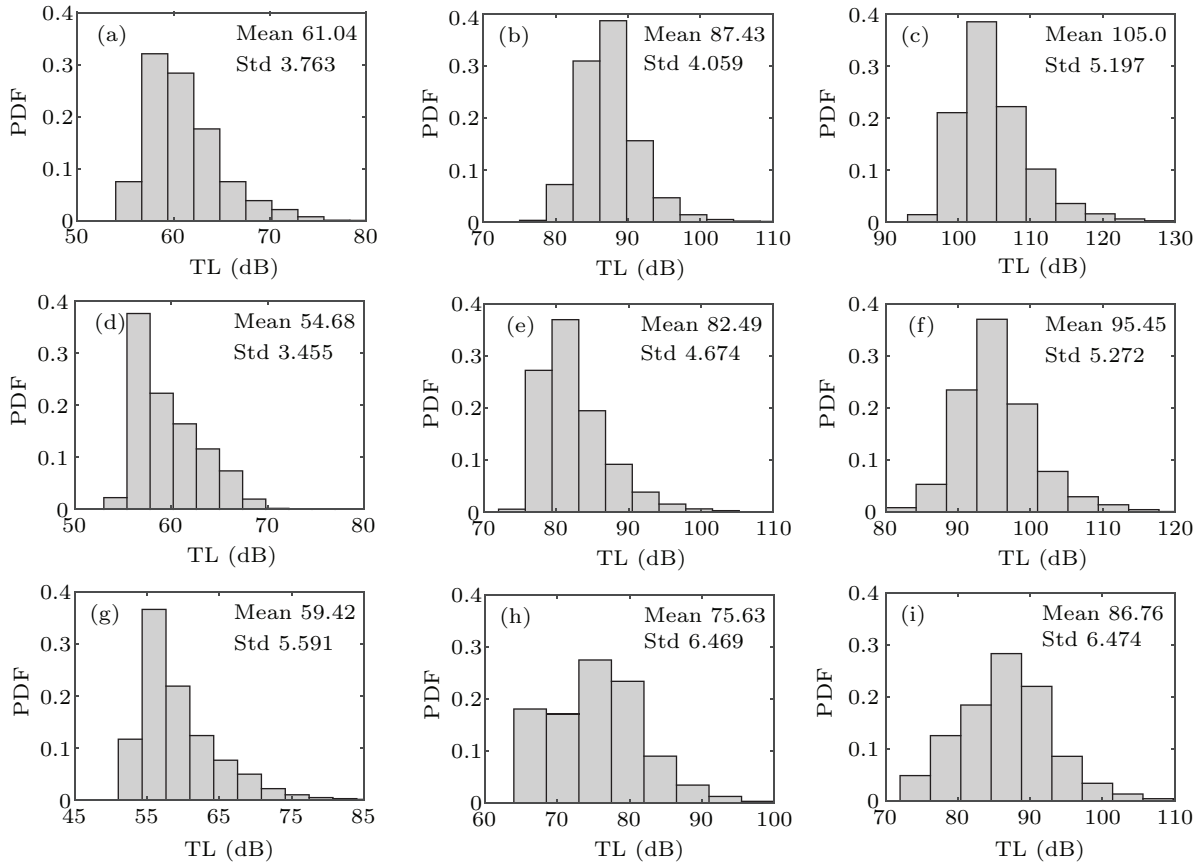


Fig. 12. PDFs of the TL for the source depth 60 m: (a)–(c) receiver range 1 km, depth 10 m, 60 m, and 100 m; (d)–(f) receiver range 4 km, depth 10 m, 60 m, and 100 m; (g)–(i) receiver range 7 km, depth 10 m, 60 m, and 100 m.

4. Discussion

For the ocean-acoustic joint model, the range-dependent waveguide environment is characterized by a continental slope and dynamic internal waves. The coupled normal mode theory is suitable for revealing its physical mechanisms of the TL sensitivity and uncertainty. The acoustic pressure $p(r,z)$ of angular frequency ω in 2D cylindrical coordinates can be decomposed into L propagation modes:[40,41]

$$p(r,z) = \sum_{l=1}^{L} A_l(r)\phi_l(r,z), \tag{9}$$

where L is the total number of normal modes. A_l and $\phi_l(r,z)$ are the lth mode amplitude and eigenfunction, respectively. To subdivide the horizontal range into Q range-dependent segments, the mode eigenfunction ϕ_l^q can be obtained by the local equation:

$$\frac{1}{\rho_0}\frac{\partial}{\partial z}\left(\frac{1}{\rho_0}\frac{\partial \phi_l^q}{\partial z}\right) + \left[\frac{\omega^2}{c_q^2(z)} - \left(k_l^q\right)^2\right]\phi_l^q = 0, \tag{10}$$

where q is the segment number, k_l^q and c^q is the local eigenvalue and sound speed in the segment q, and ρ_0 is the density. The mode amplitude A_l^{q+1} can be express as

$$A_l^{q+1} = \sum_{d=1}^{L} C_{l,d}^{q+1} H_d^q(r_q) A_d^q, \tag{11}$$

where $C_{l,d}^{q+1}$ and $H_d^q(r_q)$ are the coupled coefficient and Hankel function, respectively. For a point source in the cylindrical geometry, the initial amplitude A_l^1 is

$$A_l^1 = \frac{\mathrm{i}}{\sqrt{k_l^1}} 2\pi \phi_l^1(z_s), \tag{12}$$

where z_s is the source depth. By combining Eqs. (9)–(12) and integrating over the Q segments, the mode amplitude A_l^q and the sound field $p(r,z)$ can be obtained.

According to the coupled mode theory, the source depth affects the acoustic TL through the initial amplitude (Eq. (12)). The eigenfunctions and sound fields of different normal modes are shown in Fig. 13, which are calculated using the coupled mode model. In the calculations, the sound speed field given in Fig. 5(b) is used.

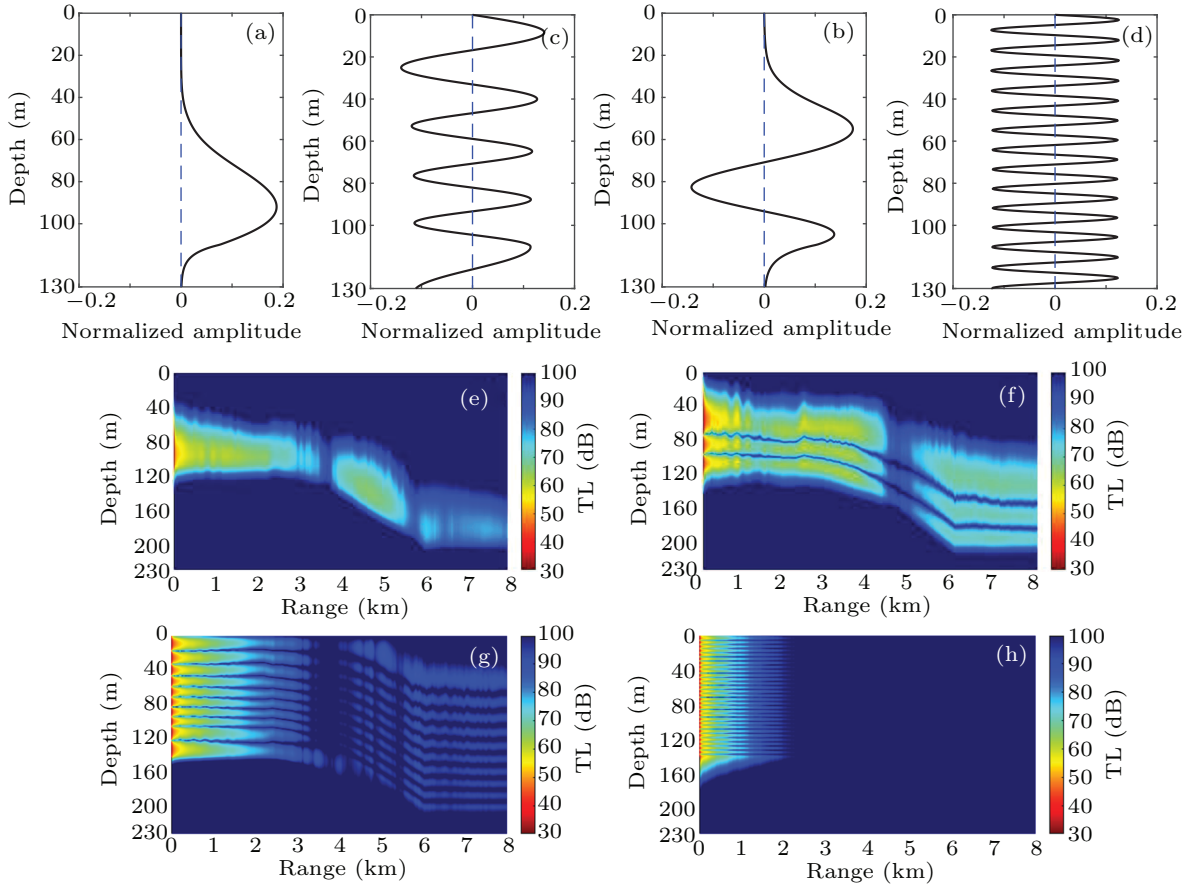


Fig. 13. Eigenfunctions and sound fields for different normal modes: [(a), (e)] mode 1; [(b), (f)] mode 3; [(c), (g)] mode 10; [(d), (h)] mode 30. In panels (a)–(d), the black solid lines and blue dashed lines represent the real and imagine parts of the eigenfunctions, respectively.

The vertical structure of the eigenfunctions of lower-order modes are affected more significantly by the sound speed profile of the water volume than the higher-order modes (Figs. 13(a)–13(d)). On the one hand, the small variation of the sound source depth (i.e., $\xi_2(t) \in [-5,5]$), caused by the dynamic ocean environment, mainly affect the initial ampli-

tude of the higher-order modes, while the effect on the lower-order modes is less. On the other hand, the sound field for the higher-order modes attenuates rapidly with range (Figs. 13(e)–13(h)). Therefore, among the three environmental parameters, the source depth variation is the main factor contributing to the acoustic propagation uncertainty in the near field.

The internal waves affect the sound field intensity through the mode amplitude $A_l(r)$ and the mode eigenfunction $\phi_l(r,z)$ [see Eq. (9)]. The horizontal sound speed gradient, caused by the internal waves, makes the local modes between two adjacent segments q and $q+1$ do not satisfy the orthogonality property, and the energy is transferred between different modes.[42–44] The energy attenuation rates of different mode are different. Thus, the internal wave causes perturbations to the sound field intensity.

On the one hand, the mode amplitude $A_l(r)$ determines the variation characteristics of the sound field intensity with range. The depth-averaged sound field intensity $I(r)$ is used to quantify the overall intensity of the sound field, which can be given by

$$I(r) = 20\log_{10}\left(\frac{1}{L}\sqrt{\sum_{l=1}^{L} A_l(r)A_l^*(r)}\right), \tag{13}$$

where * represents the conjugation. We calculate the depth averaged intensity for different times, which is shown in Fig. 14. It is seen that the difference in the depth averaged intensity of different time increases with range. In other words, the TL std caused by the internal waves increases with acoustic propagation range, which corresponds the features of the 1st Sobol index in Fig. 7(a) and the std of the uncertainty in Figs. 9 and 10.

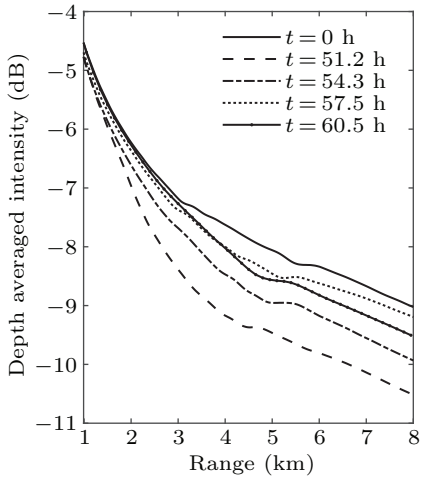


Fig. 14. Depth averaged intensity versus range at different times: $t = 0$ h represents environment without internal waves, while $t = 51.2$ h, $t = 54.3$ h, $t = 57.5$ h and $t = 60.5$ h represent the internal wave environments shown in Fig. 5.

On the other hand, the mode eigenfunction $\phi_l(r,z)$ affects the vertical distribution of the sound field. The sound field intensity in the middle and the far field is mainly contributed by the lower-order modes (Figs. 13(e)–13(h)). However, the lower-order mode eigenfunction $\phi_l(r,z)$ approaches zero above the thermocline (Figs. 13(a)–13(b)), which is strongly influenced by the water stratification. Therefore, the sound field above the thermocline is less affected by the internal waves, which leads to a smaller std of TL in the shallow layer than that in the deep layer in Fig. 11.

5. Summary and conclusions

We have studied the uncertainties of acoustic propagation and corresponding physical mechanisms in dynamic internal wave environments with continental slopes in shallow water (110–200 m). The ocean-acoustic joint model including three parts is first developed. The ocean model is configured to provide high resolution dynamic internal wave data for input to an acoustic model for range-dependent waveguides, the joint module is used to convert CTD data to sound speed and interpolate them, and the sound field is calculated using the acoustic model. The dynamic waveguide environment with imperfect information is idealized to be contributed by three uncertain parameters, i.e., internal wave, source depth, and water depth. Then the TL sensitivities to the three parameters are analyzed using the Sobol method. The mean and std of the TL are calculated using time domain Monte Carlo samplings of the uncertain parameters, for a source frequency of 300 Hz within the range 0–8 km. Finally, the physical mechanisms of the sensitivity and uncertainty of the TL are further elaborated by the coupled mode theory. Several principal conclusions are obtained as follows:

(i) Source depth is the main factor affecting the acoustic propagation uncertainties in the near field (within several hundred meters), which has great influence on the initial amplitudes of higher-order acoustic modes. In the middle and far fields (from several hundreds of meters to 8 km), the uncertainties are mainly caused by the internal waves, through the modes coupling and energy transfer.

(ii) In the vertical direction, the TL of the shallow layer is less affected by the internal waves, and the std of TL of the shallow layer is smaller than that of the deep layer. In the horizontal direction, the difference in depth-averaged intensity due to internal waves at different moments increases with the distance of acoustic propagation, and the std of TL in the near field is smaller than that in the middle and far fields.

It should be noted that the internal wave simulations are for the common scenario of a continental slope interacting with tide current, but not for a specific internal wave process in a specific sea area. The simulation results are consistent with the basic general characteristics of the internal waves. For acoustic study purpose, the numerical ocean model is an excellent support. With appropriate configuration for specific

environmental scenarios, the ocean model is capable to provide dynamic environmental data.

In addition, the variation of the source depth caused by the internal waves is far less than that for water depth. In the future work, we will estimate real dynamic ocean state and study its effects on the acoustic propagation and sonar detection performance using the ocean-acoustic joint model.

Acknowledgements

Project supported by the National Key Research and Development Program of China (Grant No. 2020YFA0607900), the National Natural Science Foundation of China (Grant Nos. 42176019 and 11874061), and the Youth Innovation Promotion Association CAS (Grant No. 2021023).

References

[1] Whalen C B, Lavergne C D, Garabato N A C, Klymak J M, Mackinnon J A and Sheen K L 2020 *Nature* **1** 606
[2] Guo C and Chen X 2014 *Prog. Oceanogr.* **121** 7
[3] Gerdes F and Finette S 2012 *J. Acoust. Soc. Am.* **132** 2251
[4] Sha L W and Nolte L W 2005 *J. Acoust. Soc. Am.* **117** 1942
[5] Dossot G A, Smith K B, Badiey M, Miller J H and Potty G R 2019 *J. Acoust. Soc. Am.* **146** 1875
[6] Chiu C S, Ramp S R, Miller C W, Lynch J F, Duda T F and Tang T Y 2004 *IEEE J. Ocean. Eng.* **29** 1249
[7] Abbot P, Dyer I and Emerson C 2006 *IEEE J. Ocean. Eng.* **31** 368
[8] Emerson C, Lynch J F, Abbot P, Lin Y T, Duda T F, Gawakiewicz G G and Chen C F 2015 *IEEE J. Ocean. Eng.* **40** 1003
[9] Da L L, Guo W H, Zhao J X and Fan P X 2015 *Acta Acust.* **40** 477 (in Chinese)
[10] DeCourcy B J, Lin Y T and Siegmann W L 2018 *J. Acoust. Soc. Am.* **143** 706
[11] Lermusiaux P F J, Xu J S and Chen C F 2010 *IEEE J. Ocean. Eng.* **35** 895
[12] James K R and Dowling D R 2008 *J. Acoust. Soc. Am.* **124** 1465
[13] Khazaie S, Wang X, Komatitsch D and Sagaut P 2019 *Wave Motion* **91** 102390
[14] Finette S 2009 *J. Acoust. Soc. Am.* **126** 2242
[15] Yang T C 2013 *J. Acoust. Soc. Am.* **135** 610
[16] Worcester P F, Andrew R K, Baggeroer A B, Colosi J A, D'Spain G L. Dzieciuch M A, Heaney K D, Howe B M, Brue M H, Kemp J N, Mercer J A, Stephen R A and Uffelen L J V 2012 *J. Acoust. Soc. Am.* **131** 3352
[17] Liu J, Peng Z H, Li Z L, Luo W Y and Yang X S 2020 *J. Acoust. Soc. Am.* **147** EL209
[18] Powell B S, Kerry C G and Cornuelle B D 2013 *J. Acoust. Soc. Am.* **134** 3211
[19] Geyer F, Sagen H, Cornuelle B, Mazloff M R and Vazquez H J 2020 *J. Acoust. Soc. Am.* **147** 1042
[20] Storto A, Falchetti S, Oddo P, Jiang Y M and Tesei A 2020 *J. Geophysi. Res. Oceans* **125** e2019JC015636
[21] Lam F P A, Jr P J H, Jannmaat J, Lermusiaux P F J, Leslie W G, Schouten M W, Raa L A and Rixen M 2009 *J. Marine Syst.* **78** S306
[22] Warn-varnas A C, Chin-bing S A, King D B, Hallock Z and Hawkins J A 2003 *Surv. Geophys.* **24** 39
[23] Duda T F, Lin Y T, Newhall A E, Helfrich K R, Lynch J F, Zhang W G, Lermusiaux P F J and Wilkin J 2019 *J. Acoust. Soc. Am.* **146** 1996
[24] Duda T F and Cornuelle B D 2021 *Proc. Meet. Acoust.* **43** 002001
[25] Huang X M, Huang X and Wang D 2019 *Geosci. Model. Dev.* **12** 4729
[26] Lin Y L, Huang X M and Liang Y S 2020 *J. Adv. Model. Earth Syst.* **12** e2019MS002036
[27] Alford M H, MacKinnon J A, Smmons H L and Nash J D 2016 *Annu. Rev. Mar. Sci.* **8** 95
[28] Chen C T and Millero F J 1977 *J. Acoust. Soc. Am.* **62** 1129
[29] Collins M D 1993 *J. Acoust. Soc. Am.* **93** 1736
[30] Tielburger D, Finette S and Wolf S 1997 *J. Acoust. Soc. Am.* **101** 789
[31] Liu R Y and Li Z L 2018 *Chin. Phys. B* **28** 014302
[32] Guo C, Chen X, Vlasenko V and Stashchuk N 2011 *Ocean Model.* **38** 203
[33] Vlasenko V and Stashchuk N 2021 *Ocean Model.* **160** 101767
[34] Buijsman M C, Kanarska Y and McWilliams J C 2010 *J. Geophys. Res.* **115** C2012
[35] Xu J X, Chen Z W, Xie J S and Cai S Q 2016 *Commun. Nonlinear Sci.* **32** 122
[36] Nakamura T, Awaji T, Hatayama T, Akitomo K, Takizawa T, Kono T, Kawasaki Y and Fukasawa M 2000 *J. Phys. Oceanography* **30** 1622
[37] Li D, Chen X and Liu A 2011 *Ocean Model.* **40** 105
[38] Sobol I M 1993 *Math Modeling Comput. Exp.* **1** 407
[39] Gao F, Xu F H, Li Z L and Qin J X 2022 *Acta Phys. Sin.* **71** 204301 (in Chinese)
[40] Jensen F B, Kuperman W A, Porter M B and Schmidt H 2011*Computational Ocean Acoustics* (New York: Springer) pp. 403–408
[41] Porter M B 1991 *The KRAKEN Normal Mode Program* (La Spezia: SACLANT Undersea Research Centre) Technical report SM-2
[42] Rouseff D, Turgut A, Wolf S N, Finette S, Orr M H, Pasewark B H, Apel J R, Badiey M, Chiu C S, Headrick R H, Lynch J F, Kemp J N, Newhall A E, von der Heydt K and Tielbuerger D 2002 *J. Acoust. Soc. Am.* **111** 1655
[43] Ren C, Huang Y W and Xia Z 2022 *Acta Phys. Sin.* **71** 024301 (in Chinese)
[44] Mo Y X, Piao S C and Zhang H G Li L 2014 *Acta Phys. Sin.* **63** 214302 (in Chinese)